An integrative systems biology and experimental approach identifies convergence of epithelial plasticity, metabolism, and autophagy to promote chemoresistance

Shengnan Xu[1], Kathryn E. Ware[1], Yuantong Ding[2], So Young Kim[3], Maya Sheth[1], Sneha Rao[4], Wesley Chan[1], Andrew J. Armstrong[1,5], William C. Eward[4], Mohit K. Jolly[6,7]*, and Jason A. Somarelli[1]*.

[1]Duke Cancer Institute and the Department of Medicine, Duke University Medical Center, Durham, NC, 27710; [2]Department of Biology, Duke University Medical Center, Durham, NC, 27710; [3]Department of Molecular Genetics and Microbiology, Duke University Medical Center, Durham, NC,2 7710; [4]Department of Orthopaedic Surgery; [5]Solid Tumor Program and the Duke Prostate Center, Duke University Medical Center, Durham, NC, 27710, USA; [6]Center for Theoretical Biological Physics, [7]Department of Bioengineering, Rice University, Houston, TX 77005-1827, USA;

*Address correspondence to jason.somarelli@duke.edu or mkjolly.15@gmail.com

Keywords. Evolution, systems biology, autophagy, lung cancer, epithelial-mesenchymal transition, tumor invasiveness, metabolism

Abstract

The evolution of therapeutic resistance is a major cause of death for patients with solid tumors. The development of therapy resistance is shaped by the ecological dynamics within the tumor microenvironment and the selective pressure induced by the host immune system. These ecological and selective forces often lead to evolutionary convergence on one or more pathways or hallmarks that drive progression. These hallmarks are, in turn, intimately linked to each other through gene expression networks. Thus, a deeper understanding of the evolutionary convergences that occur at the gene expression level could reveal vulnerabilities that could be targeted to treat therapy-resistant cancer. To this end, we used a combination of phylogenetic clustering, systems biology analyses, and wet-bench molecular experimentation to identify convergences in gene expression data onto common signaling pathways. We applied these methods to derive new insights about the networks at play during TGF-β-mediated epithelial-mesenchymal transition in a lung cancer model system. Phylogenetics analyses of gene expression data from TGF-β treated cells revealed evolutionary convergence of cells toward amine-metabolic pathways and autophagy during TGF-β treatment. Using high-throughput drug screens, we found that knockdown of the autophagy regulatory, ATG16L1, re-sensitized lung cancer cells to cancer therapies following TGF-β-induced resistance, implicating autophagy as a TGF-β-mediated chemoresistance mechanism. Analysis of publicly-available clinical data sets validated the adverse prognostic importance of ATG16L expression in multiple cancer types including kidney, lung, and colon cancer patients. These analyses reveal the usefulness of combining evolutionary and systems biology methods with experimental validation to illuminate new therapeutic vulnerabilities.

Introduction

Mammalian cells respond to external stimuli through a coordinated system of signaling and gene expression circuitry. The inputs to this system are often the ligands for receptors, which initiate signaling cascades that ultimately lead to changes in gene expression. A cell can receive, process, and integrate multiple simultaneous inputs and respond to them with a coordinated phenotypic response [1, 2].

Deregulation of the cellular signaling/response circuitry is a fundamental theme in cancer at both the tissue and single-cell levels. Indeed, deregulated intracellular signaling/gene expression circuitry is fundamental to many cancer hallmarks [3], including sustaining proliferation [4, 5], evading growth suppression [5], inducing angiogenesis [5], tumor-promoting inflammation[5], invasion [6], and metastasis [7-9].

One well-studied signaling/expression circuit that is frequently dysregulated in cancer is the transforming growth factor β (TGF-β)/SMAD axis. The TGF-β/SMAD axis is a critical developmental pathway that controls differentiation and proliferation[10]. TGF-β/SMAD signaling is also important in wound healing and fibrosis (reviewed in [11, 12]). One of the major phenotypic outputs of TGF-β/SMAD signaling is the phenotypic switch from an epithelial to a mesenchymal state, known traditionally as epithelial-mesenchymal transition (EMT) (reviewed in [13]). In the context of cancer, TGF-β-mediated EMT promotes downregulation of cell-cell adhesion and upregulation of migration and invasion [14, 15]. This pro-invasive phenotype is usually activated at the expense of proliferation [15, 16]: TGF-β induces potent cell cycle arrest through SMAD-mediated transcriptional activation of the cell cycle repressor, p21 [17]. TGF-β

76 also reprograms cellular metabolism [18] and induces autophagy [19]—a process
77 in which a cell self-digests its proteins and organelles. In addition to its cell
78 autonomous role in promoting invasiveness, TGF-β also acts non-cell
79 autonomously to create a tumor microenvironment more permissive to tumor
80 growth [20, 21]. These mechanisms can often drive resistance to chemotherapy
81 and multiple targeted therapies [22, 23].
82 However, the abovementioned effects of TGF-β/SMAD-induced EMT are
83 typically studied in isolation with focus on a few nodes of the pathway, hence
84 neglecting the effects of crosstalk among multiple signaling pathways. Such
85 crosstalk can often generate feedback loops with nonlinear dynamics, giving rise
86 to emergent, complex, and non-intuitive behavior [24]. Hence, a systems biology
87 approach integrating computational and experimental components can be
88 essential to elucidating the dynamics of underlying interconnected cellular
89 circuitry and identifying the fundamental organizational principles driving tumor
90 progression [25]. Here we used such an approach, incorporating multiple systems
91 biology tools to analyze the dynamics of TGF-β-mediated EMT and to
92 experimentally validate the computationally-derived insights (**Figure 1**).
93 Cancer progression is an evolutionary process of selection over time [26,
94 27]. Therefore, we postulated that tools developed for tracing evolutionary
95 histories may provide new insights. One of the most commonly-used methods of
96 inferring ancestral relationships is phylogenetics. Phylogenetics uses a data
97 matrix of character states to infer evolutionary relationships between groups
98 [28]. Although phylogenetics was originally developed to reconstruct ancestral
99 relationships between species, phylogenetic inference has also been applied to

diverse data sets for which no underlying ancestral relationships exist, such as geography, linguistics, or astrophysics [28].

Given the flexibility of phylogenetics as a clustering tool for multiple data types and contexts, we hypothesized that analysis of time-course gene expression data could provide crucial information about how circuits are integrated to lead to a given phenotype. We identified a convergence of gene expression data on amine metabolism pathways following TGF-β-induced EMT, and validated up-regulation of ammonia production using wet bench experimentation. Interestingly, we also identified ATG16L1, a regulator of autophagy, as a central node in an ammonia production gene network, suggesting connections between elevated amine metabolism, EMT, and autophagy. ATG16L1 was also found to be upregulated during TGF-β-induced EMT. Finally, using high throughput drug screens, we showed that siRNA-mediated inhibition of the autophagy regulator, ATG16L1, rescued TGF-β-mediated chemo-resistance. Together, this iterative combination of systems-based analyses and experimental validations suggests that TGF-β-mediated EMT converges on a gene expression network to induce autophagy and altered metabolism that can be therapeutically targeted to overcome chemoresistance.

Results

Phylogenetics analyses provide a simple and reliable tool to visualize gene expression dynamics

To test the feasibility and effectiveness of using phylogenetics as a clustering tool to analyze gene expression data, we tested if phylogenetic trees could recapitulate the temporal order of gene expression data collected at different time points. To do this, we constructed dendograms from publicly-available microarray data for immortalized prostate cells collected every 10 passages from 0 to 80 passages (GSE23038, [29]).

We first used distance-based trees to infer temporal relationships among the samples. We first used distance-based trees to infer temporal relationships among the samples. Distance-based trees use a data matrix comprised of gene expression values as a continuous variable without the need for binning gene expression data into categorical variables of being upregulated, unchanged, and downregulated. Distance-based construction of a rooted tree with root at passage 0 produced a tree topology that, with the exception of passage 70, clustered samples according to their temporal order from passage 10 to 80 (**Figure 2A**).

We also analyzed GSE23038 [29] using maximum-likelihood and parsimony phylogenetics methods. The raw data matrix was converted into three character states based on a neutral evolution model, JC69, before being used as input for these two methods of tree construction. Importantly, for all three methods, trees constructed using gene expression data recapitulated the known temporal structure of the data with robust bootstrap support (**Figure 2A-C**, bootstrap values indicated above branches). A comparison of the three cladistical

150 methods with clustering revealed that hierarchical clustering was unable to
151 accurately reconstruct the temporal order of passages (**Figure 2D-E**).
152 Similarly, we performed phylogenetic clustering on additional data sets
153 where samples had been analyzed longitudinally, including GSE17708 [30],
154 microarray data from A549 lung adenocarcinoma cells treated with TGF-β over a
155 period of 72 hours, and GSE12548, microarray data from human ARPE-19 retinal
156 pigment epithelium cells treated with TGF-β and TNF-α over 60 hours [31]. For
157 both of these data sets, phylogenetic clustering reconstructed the temporal order
158 of treatments with strong bootstrap support (**Figure 3A and B**).
159
160 *Analyzing dynamics of TGF-β treatment through visualization of tree structure*
161 *reveals two distinct temporally resolved clades*
162 A major advantage of clustering is its ability to easily visualize
163 relationships between large data sets and to derive novel useful insights. For
164 example, re-analysis of microarray data from A549 cells treated with TGF-β over
165 72 hours (GSE17708) revealed two distinctive patterns in the resulting
166 phylogenies. First, early time points (0–8 hours) were haphazardly organized in
167 clades and sub-clades, where replicates of samples were admixed, indicating that
168 phylogenetic analyses were not able to provide a clear signal based on the
169 expression data that would predict timing of treatment (**Figure 4A**). Second, the
170 later time points (≥8 hours) were well resolved, suggesting the presence of a
171 clear signal emerging in the gene expression data following long term treatment
172 with TGF-β (**Figure 4A**).
173 Consistent with a convergence of signal at later time points, RT-qPCR
174 analysis of the epithelial marker, E-cadherin, and the mesenchymal marker,

vimentin, demonstrated that E-cadherin suppression and vimentin activation were not apparent until this bifurcation of early admixed time-points vs. resolved late time-points (**Figure 4B**). Likewise, our time lapse imaging analysis of growth rate between vehicle-treated and TGF-β-treated A549 cells showed that differences in growth rate between the two conditions were not observed until ~72 hours after the initiation of treatment (**Figure 4C**), consistent with reports demonstrating that EMT induces cell cycle arrest [32, 33]. These experimental results suggest that the timing of both gene expression and phenotypic traits associated with EMT are consistent with the convergence of an emerging signal at late time points within the dendograms.

Next, we extracted genes that were differentially expressed across the two major clades of early and late treatment times. Pathway analysis of these genes showed that multiple amine-metabolism pathways were significantly altered during TGF-β treatment (**Figure 4D**). To experimentally test if ammonia metabolism was altered during TGF-β treatment, we performed ammonia production assays on A549 cells. Importantly, we found that ammonia production was altered significantly upon TGF-β treatment at later time points, with little change in ammonia production during earlier time points (**Figure 4E**). Together, these analyses demonstrated the utility of simple visualizations, such as phylogenetic trees and clustering dendograms, to yield new testable hypotheses.

Gene expression networks couple ammonia production to autophagy

Previous research has identified a connection between up-regulation of ammonia production and induction of autophagy (7). Based on this connection, we tested if TGF-β-induced EMT led to an increase in autophagy markers. In

support of this hypothesis, TGF-β treatment led to upregulation of autophagy markers LC3A/B and ATG16L1 (**Figure 5A**). To better understand the connections between ammonia production and autophagy, we used Cytoscape to construct gene regulatory networks related to amine metabolism genes and autophagy regulators. We constructed gene networks that included the ammonia production genes identified by the pathway analysis, along with the autophagy markers LC3A/B and ATG16L1 that we identified in our western blots to be activated upon TGF-β treatment. Although we found few gene-gene interactions among amine metabolism genes alone (**Figure 5B**), when we added the autophagy regulator ATG16L1 to this network, it connected the entire set of previously-isolated amine metabolism sub-networks (**Figure 5C**). LC3A/B was a node in the ATG16L1 network (**Supplementary File 4**). Our results suggest that TGF-β-mediated EMT is associated with increased amine production and upregulation of autophagy. It remains to be tested in this system if the ammonia production induces autophagy, as has been demonstrated previously in both yeast and mouse embryonic fibroblasts [34], or if TGF-β-induced autophagy upregulation leads to more ammonia. However, our results demonstrate a connection between TGF-β-mediated EMT, altered amine production, and upregulation of autophagy.

Autophagy inhibition re-sensitizes cells to TGF-β-induced chemoresistance

Our data revealed that TGF-β-induced EMT leads to ammonia production and upregulation of autophagy. Interestingly, both EMT and autophagy are known to be involved in chemoresistance. EMT can drive chemoresistance in multiple cancers [35-38]. Likewise, autophagy is a pro-survival mechanism in response to cellular stresses,

such as hypoxia and nutrient deprivation, and is increasingly implicated in resistance to cancer treatments [39, 40]. Integrating our observations with these reports, we hypothesized that EMT-induced drug resistance is mediated, at least in part, by elevated autophagy.

To test this hypothesis, we used high-throughput drug screens of 119 FDA-approved small-molecule anti-cancer agents. To do this, we first tested if TGF-β-mediated EMT led to chemoresistance. We screened A549 cells treated with either vehicle or TGF-β and plated at both low and high density. After 72 hours of incubation with each drug, the overall cell viability was analyzed with CellTiterGlo. We first performed quality control analyses of the screens. Linear regression of the empty wells and DMSO-treated wells showed virtually no relationship between the CellTiterGlo value and the position on the plate when comparing the same plate setup across multiple plates (R^2 = 0.0862), suggesting that the screen results did not suffer from plate effects (**Supplementary Figure 1**). In contrast, the correlation coefficients in drug-containing wells were greater than 0.8 between high and low cell density for both vehicle- and TGF-β-treated conditions, suggesting high reproducibility across replicate plates, when drug is present in the well (**Supplementary Figure 1**).

Given the lack of apparent plate effects and strong reproducibility between replicate screens, we investigated whether TGF-β induced chemoresistance. Consistent with our hypothesis, TGF-β treatment increased resistance to 60% (71/119) of the compounds tested, as evaluated by an increase in CellTiterGlo absorbance as compared to vehicle-treated control wells (**Figure 6A**). Analysis of these compounds by pathway targets showed that TGF-β induced resistance to both broad spectrum chemotherapies, such as microtubule-targeting agents and topoisomerase inhibitors, as well as multiple targeted therapies, including those against HER2 and EGFR (**Figure 6B**).

Next, to investigate the importance of autophagy in promoting TGF-β-induced therapy resistance, we performed siRNA-mediated knockdown of ATG16L1, the autophagy marker we identified as upregulated in TGF-β treated cells. We first tested knockdown efficiency using four independent siRNAs and selected by western blot analysis siRNA_1 for subsequent drug screens (**Figure 6C**). We then screened A549 with the same 119 drugs +/– TGF-β and treated with either a non-silencing siRNA or siRNA_1 targeting ATG16L1. Remarkably, ATG16L1 knockdown re-sensitized cells to 29/71 (41%) of drugs for which TGF-β treatment led to increased resistance (**Figure 6D**). Interestingly, these drugs included current standard of care therapies for small-cell lung cancer (SCLC), doxorubicin and topotecan, as well as anti-VEGFR therapies, regorafenib and axitinib, both of which have shown promising clinical benefits in early stage clinical trials against advanced non-small-cell lung cancer (NSCLC) [41, 42], and cabozantinib, a tyrosine kinase inhibitor that has shown efficacy along or in combination with erlotinib in treatment of EGFR wild-type NSCLC patients [43]. Analysis by pathways showed that autophagy inhibition on average re-sensitized cells to multiple targeted therapies, including c-MET, c-RET, FLT3, TAM2, and dihydrofolate reductase (DHFR) (**Figure 6E**). Together, our results support the hypothesis that TGF-β-mediated therapy resistance is driven, in part, by autophagy, suggesting the potential use of autophagy inhibitors as a concurrent or adjuvant therapy to counter resistance.

To determine if ATG16L1 was related to clinical outcomes, we analyzed ATG16L1 expression in gene expression data sets from patient tumors. Analysis of Kaplan Meier curves showed that low ATG16L1 expression is prognostic for improved overall survival in patients with lung and clear cell renal cancer (**Figure 7A–C**) and improved relapse-free survival in patients with colorectal cancer (**Figure 7D**). It is also worth noting that high ATG16L1 was prognostic for improved disease-free survival in

breast cancer (**Figure 7E**). However, despite the opposite trend in breast cancer, these analyses indicate ATG16L1 as an important prognostic marker of clinical response and cancer cell aggression.

Discussion

The progression of cancer from an indolent, slow-growing primary tumor to metastatic and therapy resistant disease is, at its foundation, an evolutionary process. Genetic and genomic dysregulation promotes heterogeneity in tumor cell populations [44], which provides raw materials for selection of the fittest cancer cells. During this process, mutations [45], epigenetic alterations [46], and gene expression changes [47] are selected that enable survival of individual cancer cells under the diverse environmental pressures not only within the tumor, but also during metastatic progression [48, 49] and the emergence of therapy resistance [50].

Here, we combined methods rooted in evolutionary theory, such as phylogenetic inference, with pathway and network analyses, as well as experimental techniques, to yield new insights. By taking this novel approach to analyze a well-established system—TGF-β-induced EMT—we identified mechanisms of therapy resistance. Specifically, we found that EMT leads to increased production of intracellular ammonia. Ammonia is a by-product of protein breakdown and serves an important function in maintaining homeostasis in electrolyte concentration [51]. Recent evidence, however, also suggests that ammonia production is involved in regulating autophagy and pro-survival circuits that contribute to chemoresistance [34, 52]. Importantly, autophagy can lead to increased aggressiveness in cancer, perhaps as an adaptive response to cellular

300 stress. In our present study, downregulation of autophagy partially reversed
301 EMT-induced therapy resistance, suggesting the potential benefits of concurrent
302 uses of autophagy inhibitors with standard-of-care therapies.
303 TGF-β has also been reported to induce metabolic reprogramming of
304 stromal cells such as cancer-associated fibroblasts (CAFs), where CAFs
305 overexpressing TGF-β ligands show increased autophagy and HIF-1α activation,
306 and concomitant reduced oxidative phosphorylation [53]. The
307 scaffolding/regulatory protein caveolin-1 – a functional regulator of TGF-β
308 signaling – can play a key role in coordinating these responses [54, 55]. Thus, the
309 nexus of TGF-β signaling, increased autophagy, and metabolic reprogramming
310 may be a common design principle of multiple cell types.
311 Interestingly, inhibition of autophagy consistently led to re-sensitization to
312 c-Met inhibitors during EMT. The c-Met oncogene is one of the two most highly
313 mutated tyrosine kinase receptors in NSCLC, and resistance to tyrosine kinase
314 inhibitors (TKI) invariably follows after treatment [56]. Indeed, resistance to
315 erlotinib is common in lung cancer, and ATG16L1 knockdown re-sensitized cells
316 to increased EMT-induced erlotinib resistance. EMT has been shown as an
317 important contributor to this resistance as TKI resistance NSCLC cell lines has a
318 more mesenchymal phenotype, higher expression of mesenchymal markers such
319 as Zeb-1 and vimentin, and downregulation of E-cadherin [57]. Recent evidence
320 has shown that c-Met promotes anoikis-resistance and cell growth via activation
321 of autophagy regulators, such as ATG5 and Beclin-1 [58]. These observations
322 suggest that autophagy may be an important resistance mechanism and a
323 combinatorial use of autophagy inhibitors with TKIs may increase therapeutic
324 efficacy of TKIs and possibly prolong or reverse resistance.

Materials and Methods

Cell Culture

All cell lines were obtained from the Duke Cell Culture Facility. The Duke Cell Culture Facility routinely tests for mycoplasma and performs cell line authentication by short tandem repeat analysis. Cells were cultured in Dulbecco's Modified Eagle Medium (DMEM) with fetal bovine serum (FBS) and 1% penicillin-streptomycin in a standard 37 °C tissue culture incubator with 5% CO_2.

RNA extraction, reverse transcription, and RT-qPCR

RNA extraction, reverse transcription, and RT-qPCR were performed as previously described [59].

Western blotting

Cells were prepared and lysed in 1x radio-immunoprecipitation assay (RIPA) buffer mixed with 1x protease and phosphatase inhibitor cocktail (Roche). Cell lysates were incubated at 4°C for 20 minutes and centrifuged at 14,000 x g for 5 minutes. Cleared lysates were mixed with 4x Laemmli loading buffer and incubated at 95°C for 3 minutes. Lysates were separated in 4–12% NuPAGE Novex Bis-Tris gels (ThermoFisher). Proteins were transferred to nitrocellulose membrane (GE Healthcare Life Sciences) in 1x NuPAGE Transfer Buffer (ThermoFisher) for 2 hours at 75V at 4°C in the cold room. Membranes were blocked at room temperature using Starting Block T20 TBS Blocking Buffer (ThermoFisher). Primary antibodies were added to the blocking buffer and incubated at 4°C overnight. Membranes were washed two times for 5 minutes

each with phosphate buffered saline (PBS) and incubated with Licor goat anti-mouse or goat anti-rabbit secondary antibodies diluted 1:20,000 in Starting Block buffer. Membranes were visualized using the Odyssey Fc imager (27402864). Primary antibodies used included GAPDH (C2415, Santa Cruz Biotechtology), ATG16L1 (8089T, Cell Signaling) and LC3 A/B (12741T, Cell Signaling) at 1:1000.

Ammonia Production Assay

A total of 200,000 cells were seeded in 6-cm dishes. At each time point, cells were washed with PBS, scraped, and lysed in Ammonia Assay Buffer provided in the Abcam ammonia assay kit (ab83360) after the end of each treatment time point. Ammonia production assays were performed after collecting all time points using the protocol recommended by the manufacturer.

Cytoscape analysis

Gene networks were analyzed by importing all available human data on each gene in the Universal Interaction Database Client using Cytoscape version 3.5.1. All relevant networks of genes were merged to visualize interactions among genes. The Cytoscape files used to construct the networks are provided as merged networks 5 and 6 in Supplementary File 4.

Phylogenetic reconstructions from gene expression data

Distance-based dendogram analyses were performed by constructing a distance matrix calculated based on the entire microarray data set for each data set to be analyzed, using the genes as the characters, the raw expression value for each gene as the character states, and the samples as the taxa. The Neighbor

375 Joining method [60] was used for reconstructing phylogeny with distance
376 matrices. To perform analysis based on maximum-likelihood (ML) and
377 parsimony, the continuous gene expression data was converted into categorical
378 variables. For example, for GSE23038, we used the passage 0 sample as an
379 'outgroup', and converted the gene expression data for all other samples into
380 either up-regulated, down-regulated, or constant relative to passage 0. The
381 reliability of the parsimony method is generally considered to increase with an
382 increasing number of informative characters [61-63]. Therefore, cut-off
383 thresholds of up- and down-regulation were determined by calculating the
384 maximum number of informative sites given different cut-offs, and a threshold
385 was selected that provided the highest number of informative sites in each data
386 set. ML and parsimony analyses were then performed based on converted data.
387 ML analysis after data conversion was performed online on a free phylogeny
388 platform PhyML 3.0 (14) whereas distance and parsimony tree constructions
389 were performed using the APE [64] and Phangorn [65] packages implemented in
390 R (15). Bootstrap tests of 100 pseudo-replicates were performed for all
391 phylogenies to assess the branch support. Tree files were visualized in FigTree
392 (Andrew Rambaut; http://tree.bio.ed.ac.uk/software/figtree/).
393
394 *High-throughput screening*
395 A549 cells were screened with the NCI Approved Oncology Drugs Set VI in the
396 presence of vehicle (4 mM HCl and 2% BSA) or 4 ng/mL recombinant human
397 TGF-β (R&D Systems). Briefly, A549 cells were dispensed using liquid handling
398 into 384 well plates with no drug, DMSO, or 1 μM drug at cell plating densities of
399 250 and 1000 cells/well. Plates were incubated at 37°C, and cell viability was

assayed by CellTiterGlo after 72 hours. Relative drug resistance or sensitivity was calculated as the fold change difference in CellTiterGlo value between vehicle-treated and TGF-β-treated wells. To perform the screen in the context of ATG16L1 knockdown, 20 nM siRNA targeting ATG16L1 was delivered to A549 cells by reverse transfection using RNAiMax and incubated at 37°C for 24 hours. After 24 hours, the drug screen was performed -/+ TGF-β as described above. All screens were performed in the Duke Functional Genomics Shared Resource.

Correlation of ATG16L1 with clinical outcomes

Kaplan Meier curves were generated based on patients stratified by ATG16L1 expression level using R2: Genomics Analysis and Visualization Platform (https://hgserver1.amc.nl/cgi-bin/r2/main.cgi) and GEPIA (http://gepia.cancer-pku.cn/). The scan option was used to automatically select the cut-off values in the R2 platform, and default settings were used for GEPIA.

Acknowledgements

JAS wishes to acknowledge support from Meg and Bill Lindenberger, the Paul and Shirley Friedland Fund, the Triangle Center for Evolutionary Medicine, and funds raised in memory of Muriel E. Rudershausen (riding4research.org). The authors wish to thank Dr. Jeffrey Townsend and Dr. Herbert Levine for many helpful discussions in preparation of the manuscript. MKJ is supported by a training fellowship from the Gulf Coast Consortia on Computational Cancer Biology Training Program (CPRIT Grant No. RP170593).

Figure Legends

Figure 1. An integrated framework of iterative systems-level analysis and experimental validation provides new insights. Large amounts of raw data, generated by new experimentation or re-analyzed from public databases (1), are analyzed by clustering approaches to easily visualize data topology (2). This visualization fosters new, deeper understanding that informs a new hypothesis (3). Experimental validation of the new hypothesis generates new data (4), which is analyzed and visualized as a system (5).

Figure 2. Phylogenetic reconstruction provides a simple visualization tool to view temporal changes in gene expression data. A. Distance-based phylogeny of GSE23038; serial passage of normal prostate cells immortalized with hTERT using gene expression data as a continuous variable. **B.** Maximum-likelihood and **C.** Maximum parsimony trees constructed based on gene expression data transformed to categorical variables. **D.** Single and **E.** Complete linkage hierarchical clustering provides similar groupings of passage numbers, but lacks the temporal structure.

Figure 3. Phylogenetic clustering enables reconstruction of longitudinal data based on gene expression. A. Distance, maximum parsimony, and maximum-likelihood dendograms of GSE17708; microarray analysis of A549 cells treated with TGF-β over 72 hours. **B.** Distance, maximum parsimony, and maximum-likelihood phylogeny construction of GSE12548; TGF-β and TNF-α treatment of human retinal pigment epithelium cells over 60 hours.

Figure 4. Visualization of tree topology reveals altered metabolism during epithelial-mesenchymal transition (EMT). A. The topology of the maximum-likelihood reconstruction of GSE17708 showed an admixed clade at early time points in A549 cells with TGF-β treatment, with a clearly resolved clade of later time points after eight hours as phenotypic signal switched from epithelial to mesenchymal. **B.** Consistent with the tree topology, changes in EMT biomarkers E-cadherin and vimentin were not apparent until after eight hours of treatment. **C.** Growth curves of A549 cells treated with vehicle (blue circles) or TGF-β (red x) analyzed by IncuCyte time lapse imaging revealed TGF-β-induced growth inhibition by 48-72 hours. **D.** Pathway analysis of genes contributing to the bifurcation of early (<8 hours) and late (≥8 hours) time point clades revealed TGF-β-induced changes in amine metabolism pathways at the later time points as compared to the early time points. **E.** Ammonia production assays validated the prediction that TGF-β induces up-regulation of ammonia production.

Figure 5. Epithelial-mesenchymal transition induces activation of autophagy and links to an amine production gene network. A. TGF-β-induced epithelial-mesenchymal transition led to up-regulation of autophagy markers ATG16L1 and MAP1LC3A (LC3A/B). **B.** Cytoscape networks of amine production genes identified in Figure 4 showed few interactions between sub-networks. **C.** Addition of the autophagy regulator, ATG16L1 (yellow circle), acted as a central hub to connect all amine metabolism sub-networks.

Figure 6. ATG16L1 knockdown rescues TGF-β-mediated chemo-resistance. A. A screen of 119 FDA-approved small molecule inhibitors demonstrated a broad increase

475 in chemoresistance following TGF-β treatment. Each black dot represents one
476 compound. Dots above the 1 were differentially resistant in TGF-β-treated cells as
477 compared to vehicle-treated cells; dots below the 1 were more sensitive in the TGF-β-
478 treated cells as compared to vehicle treated cells. **B.** Analysis of drug screen data by
479 targets and pathways identified increased TGF-β-mediated resistance to several
480 common chemotherapies, such as microtubule-associated and topoisomerase inhibitor
481 therapies, and targeted therapies in lung cancer treatment, such as c-MET, VEGF, and
482 EGFR (purple bars). **C.** Knockdown of ATG16L1 by siRNAs was validated by western
483 blotting. siCtrl = non-silencing siRNA; si_1, si_2, si_4, si_5 are independent siRNAs
484 targeting ATG16L1. **D.** A549 lung adenocarcinoma cells -/+ TGF-β and -/+ siATG16_1
485 were screened against 119 FDA-approved compounds to identify drugs for which
486 ATG16L1 rescued TGF-β-mediated therapy resistance. ATG16L1 knockdown re-
487 sensitized cells to multiple therapeutic agents. **E.** Pathway level analysis of compounds
488 where TGF-β-mediated resistance was rescued by ATG16L1 knockdown.
489
490 **Figure 7. ATG16L1 is a prognostic biomarker of survival and progression in**
491 **carcinoma patients. A.** Low ATG16L1 expression is prognostic for improved overall
492 survival in lung adenocarcinoma patients. **B.** Low ATG16L1 expression significantly
493 predicts improved overall survival in kidney renal clear cell carcinoma patients. **C.**
494 Lower ATG16L1 expression in lung adenocarcinoma from The Cancer Genome Atlas
495 data set is prognostic for improved overall survival; data analyzed using GEPIA -
496 http://gepia.cancer-pku.cn/. **D.** Low ATG16L1 expression trends with better relapse-
497 free survival in colorectal carcinoma patients. **E.** High levels of ATG16L1 are ATG16L1 is
498 prognostic of increased disease-free survival in breast cancer patients.
499

500 **References**

501

502 1. Chaiwanon, J., et al., *Information Integration and Communication in Plant Growth*
503 *Regulation.* Cell, 2016. **164**(6): p. 1257-1268.
504 2. Pawson, C.T. and J.D. Scott, *Signal integration through blending, bolstering and*
505 *bifurcating of intracellular information.* Nat Struct Mol Biol, 2010. **17**(6): p. 653-
506 8.
507 3. Hanahan, D. and R.A. Weinberg, *Hallmarks of cancer: the next generation.* Cell,
508 2011. **144**(5): p. 646-74.
509 4. Janda, E., et al., *Oncogenic Ras/Her-2 mediate hyperproliferation of polarized*
510 *epithelial cells in 3D cultures and rapid tumor growth via the PI3K pathway.*
511 Oncogene, 2002. **21**(33): p. 5148-59.
512 5. Sever, R. and J.S. Brugge, *Signal transduction in cancer.* Cold Spring Harb Perspect
513 Med, 2015. **5**(4).
514 6. van Golen, K.L., et al., *Mitogen activated protein kinase pathway is involved in*
515 *RhoC GTPase induced motility, invasion and angiogenesis in inflammatory breast*
516 *cancer.* Clin Exp Metastasis, 2002. **19**(4): p. 301-11.
517 7. Iqbal, W., et al., *Targeting signal transduction pathways of cancer stem cells for*
518 *therapeutic opportunities of metastasis.* Oncotarget, 2016. **7**(46): p. 76337-76353.
519 8. Janda, E., et al., *Ras and TGF[beta] cooperatively regulate epithelial cell plasticity*
520 *and metastasis: dissection of Ras signaling pathways.* J Cell Biol, 2002. **156**(2): p.
521 299-313.
522 9. Brown, W.S., et al., *Covalent Targeting of Fibroblast Growth Factor Receptor*
523 *Inhibits Metastatic Breast Cancer.* Mol Cancer Ther, 2016. **15**(9): p. 2096-106.
524 10. Kitisin, K., et al., *Tgf-Beta signaling in development.* Sci STKE, 2007. **2007**(399): p.
525 cm1.
526 11. Walton, K.L., K.E. Johnson, and C.A. Harrison, *Targeting TGF-beta Mediated SMAD*
527 *Signaling for the Prevention of Fibrosis.* Front Pharmacol, 2017. **8**: p. 461.
528 12. Carthy, J.M., *TGFbeta signaling and the control of myofibroblast differentiation:*
529 *Implications for chronic inflammatory disorders.* J Cell Physiol, 2018. **233**(1): p.
530 98-106.
531 13. Nawshad, A., et al., *Transforming growth factor-beta signaling during epithelial-*
532 *mesenchymal transformation: implications for embryogenesis and tumor*
533 *metastasis.* Cells Tissues Organs, 2005. **179**(1-2): p. 11-23.
534 14. Papageorgis, P., *TGFbeta Signaling in Tumor Initiation, Epithelial-to-Mesenchymal*
535 *Transition, and Metastasis.* J Oncol, 2015. **2015**: p. 587193.
536 15. Fuxe, J., T. Vincent, and A. Garcia de Herreros, *Transcriptional crosstalk between*
537 *TGF-beta and stem cell pathways in tumor cell invasion: role of EMT promoting*
538 *Smad complexes.* Cell Cycle, 2010. **9**(12): p. 2363-74.
539 16. Huang, S.S. and J.S. Huang, *TGF-beta control of cell proliferation.* J Cell Biochem,
540 2005. **96**(3): p. 447-62.
541 17. Moustakas, A., et al., *Mechanisms of TGF-beta signaling in regulation of cell growth*
542 *and differentiation.* Immunol Lett, 2002. **82**(1-2): p. 85-91.
543 18. Jiang, L., et al., *Metabolic reprogramming during TGFbeta1-induced epithelial-to-*
544 *mesenchymal transition.* Oncogene, 2015. **34**(30): p. 3908-16.

19. Kiyono, K., et al., *Autophagy is activated by TGF-beta and potentiates TGF-beta-mediated growth inhibition in human hepatocellular carcinoma cells.* Cancer Res, 2009. **69**(23): p. 8844-52.
20. Hazelbag, S., et al., *Transforming growth factor-beta1 induces tumor stroma and reduces tumor infiltrate in cervical cancer.* Hum Pathol, 2002. **33**(12): p. 1193-9.
21. Gigante, M., L. Gesualdo, and E. Ranieri, *TGF-beta: a master switch in tumor immunity.* Curr Pharm Des, 2012. **18**(27): p. 4126-34.
22. Yao, Z., et al., *TGF-beta IL-6 axis mediates selective and adaptive mechanisms of resistance to molecular targeted therapy in lung cancer.* Proc Natl Acad Sci U S A, 2010. **107**(35): p. 15535-40.
23. Brunen, D., et al., *TGF-beta: an emerging player in drug resistance.* Cell Cycle, 2013. **12**(18): p. 2960-8.
24. Magi, S., Iwamoto, K., and Okada-Hatakeyama, *Current status of mathematical modeling of cancer – From the viewpoint of cancer hallmarks.* Current Opinion in Systems Biology, 2017. **2**: p. 39-48.
25. Anderson, A.R. and V. Quaranta, *Integrative mathematical oncology.* Nat Rev Cancer, 2008. **8**(3): p. 227-34.
26. Gerlinger, M., et al., *Cancer: evolution within a lifetime.* Annu Rev Genet, 2014. **48**: p. 215-36.
27. Maley, C.C., et al., *Classifying the evolutionary and ecological features of neoplasms.* Nat Rev Cancer, 2017. **17**(10): p. 605-619.
28. Somarelli, J.A., et al., *PhyloOncology: Understanding cancer through phylogenetic analysis.* Biochim Biophys Acta, 2017. **1867**(2): p. 101-108.
29. Kogan-Sakin, I., et al., *Mutant p53(R175H) upregulates Twist1 expression and promotes epithelial-mesenchymal transition in immortalized prostate cells.* Cell Death Differ, 2011. **18**(2): p. 271-81.
30. Sartor, M.A., et al., *ConceptGen: a gene set enrichment and gene set relation mapping tool.* Bioinformatics, 2010. **26**(4): p. 456-63.
31. Takahashi, E., et al., *Tumor necrosis factor-alpha regulates transforming growth factor-beta-dependent epithelial-mesenchymal transition by promoting hyaluronan-CD44-moesin interaction.* J Biol Chem, 2010. **285**(6): p. 4060-73.
32. Lovisa, S., et al., *Epithelial-to-mesenchymal transition induces cell cycle arrest and parenchymal damage in renal fibrosis.* Nat Med, 2015. **21**(9): p. 998-1009.
33. Vega, S., et al., *Snail blocks the cell cycle and confers resistance to cell death.* Genes Dev, 2004. **18**(10): p. 1131-43.
34. Cheong, H., T. Lindsten, and C.B. Thompson, *Autophagy and ammonia.* Autophagy, 2012. **8**(1): p. 122-3.
35. Du, B. and J.S. Shim, *Targeting Epithelial-Mesenchymal Transition (EMT) to Overcome Drug Resistance in Cancer.* Molecules, 2016. **21**(7).
36. Singh, A. and J. Settleman, *EMT, cancer stem cells and drug resistance: an emerging axis of evil in the war on cancer.* Oncogene, 2010. **29**(34): p. 4741-51.
37. Fischer, K.R., et al., *Epithelial-to-mesenchymal transition is not required for lung metastasis but contributes to chemoresistance.* Nature, 2015. **527**(7579): p. 472-6.
38. Zheng, X., et al., *Epithelial-to-mesenchymal transition is dispensable for metastasis but induces chemoresistance in pancreatic cancer.* Nature, 2015. **527**(7579): p. 525-30.
39. Sui, X., et al., *Autophagy and chemotherapy resistance: a promising therapeutic target for cancer treatment.* Cell Death Dis, 2013. **4**: p. e838.

40. Yang, Z.J., et al., *The role of autophagy in cancer: therapeutic implications.* Mol Cancer Ther, 2011. **10**(9): p. 1533-41.
41. Schiller, J.H., et al., *Efficacy and safety of axitinib in patients with advanced non-small-cell lung cancer: results from a phase II study.* J Clin Oncol, 2009. **27**(23): p. 3836-41.
42. Mross, K., et al., *A phase I dose-escalation study of regorafenib (BAY 73-4506), an inhibitor of oncogenic, angiogenic, and stromal kinases, in patients with advanced solid tumors.* Clin Cancer Res, 2012. **18**(9): p. 2658-67.
43. Neal, J.W., et al., *Erlotinib, cabozantinib, or erlotinib plus cabozantinib as second-line or third-line treatment of patients with EGFR wild-type advanced non-small-cell lung cancer (ECOG-ACRIN 1512): a randomised, controlled, open-label, multicentre, phase 2 trial.* Lancet Oncol, 2016. **17**(12): p. 1661-1671.
44. Nowell, P.C., *The clonal evolution of tumor cell populations.* Science, 1976. **194**(4260): p. 23-8.
45. Lipinski, K.A., et al., *Cancer Evolution and the Limits of Predictability in Precision Cancer Medicine.* Trends Cancer, 2016. **2**(1): p. 49-63.
46. Feinberg, A.P., *Epigenetic stochasticity, nuclear structure and cancer: the implications for medicine.* J Intern Med, 2014. **276**(1): p. 5-11.
47. Ostrow, S.L., et al., *Cancer evolution is associated with pervasive positive selection on globally expressed genes.* PLoS Genet, 2014. **10**(3): p. e1004239.
48. Casasent, A.K., M. Edgerton, and N.E. Navin, *Genome evolution in ductal carcinoma in situ: invasion of the clones.* J Pathol, 2017. **241**(2): p. 208-218.
49. Seyfried, T.N. and L.C. Huysentruyt, *On the origin of cancer metastasis.* Crit Rev Oncog, 2013. **18**(1-2): p. 43-73.
50. Gatenby, R. and J. Brown, *The Evolution and Ecology of Resistance in Cancer Therapy.* Cold Spring Harb Perspect Med, 2018. **8**(3).
51. Kurtz, I., P.D. Dass, and S. Cramer, *The importance of renal ammonia metabolism to whole body acid-base balance: a reanalysis of the pathophysiology of renal tubular acidosis.* Miner Electrolyte Metab, 1990. **16**(5): p. 331-40.
52. Eng, C.H., et al., *Ammonia derived from glutaminolysis is a diffusible regulator of autophagy.* Sci Signal, 2010. **3**(119): p. ra31.
53. Guido, C., et al., *Metabolic reprogramming of cancer-associated fibroblasts by TGF-beta drives tumor growth: connecting TGF-beta signaling with "Warburg-like" cancer metabolism and L-lactate production.* Cell Cycle, 2012. **11**(16): p. 3019-35.
54. Razani, B., et al., *Caveolin-1 regulates transforming growth factor (TGF)-beta/SMAD signaling through an interaction with the TGF-beta type I receptor.* J Biol Chem, 2001. **276**(9): p. 6727-38.
55. Shiroto, T., et al., *Caveolin-1 is a critical determinant of autophagy, metabolic switching, and oxidative stress in vascular endothelium.* PLoS One, 2014. **9**(2): p. e87871.
56. Pasquini, G. and G. Giaccone, *C-MET inhibitors for advanced non-small cell lung cancer.* Expert Opin Investig Drugs, 2018. **27**(4): p. 363-375.
57. Rastogi, I., et al., *Mechanism of c-Met and EGFR tyrosine kinase inhibitor resistance through epithelial mesenchymal transition in non-small cell lung cancer.* Biochem Biophys Res Commun, 2016. **477**(4): p. 937-944.
58. Barrow-McGee, R., et al., *Beta 1-integrin-c-Met cooperation reveals an inside-in survival signalling on autophagy-related endomembranes.* Nat Commun, 2016. **7**: p. 11942.

642 59. Somarelli, J.A., et al., *Mesenchymal-Epithelial Transition in Sarcomas Is Controlled*
643 *by the Combinatorial Expression of MicroRNA 200s and GRHL2.* Mol Cell Biol,
644 2016. **36**(19): p. 2503-13.
645 60. Saitou, N. and M. Nei, *The neighbor-joining method: a new method for*
646 *reconstructing phylogenetic trees.* Mol Biol Evol, 1987. **4**(4): p. 406-25.
647 61. Hillis, D.M., and James J. Bull *An empirical test of bootstrapping as a method for*
648 *assessing confidence in phylogenetic analysis.* Systematic biology 1993. **42**(2): p.
649 182-192.
650 62. Wiens, J.J., *Polymorphic characters in phylogenetic systematics.* Systematic
651 biology, 1995. **44**(4): p. 482-500.
652 63. Hillis, D.M., J.P. Huelsenbeck, and C.W. Cunningham, *Application and accuracy of*
653 *molecular phylogenies.* Science, 1994. **264**(5159): p. 671-7.
654 64. Paradis, E., J. Claude, and K. Strimmer, *APE: Analyses of Phylogenetics and*
655 *Evolution in R language.* Bioinformatics, 2004. **20**(2): p. 289-90.
656 65. Schliep, K.P., *phangorn: phylogenetic analysis in R.* Bioinformatics, 2011. **27**(4): p.
657 592-3.
658

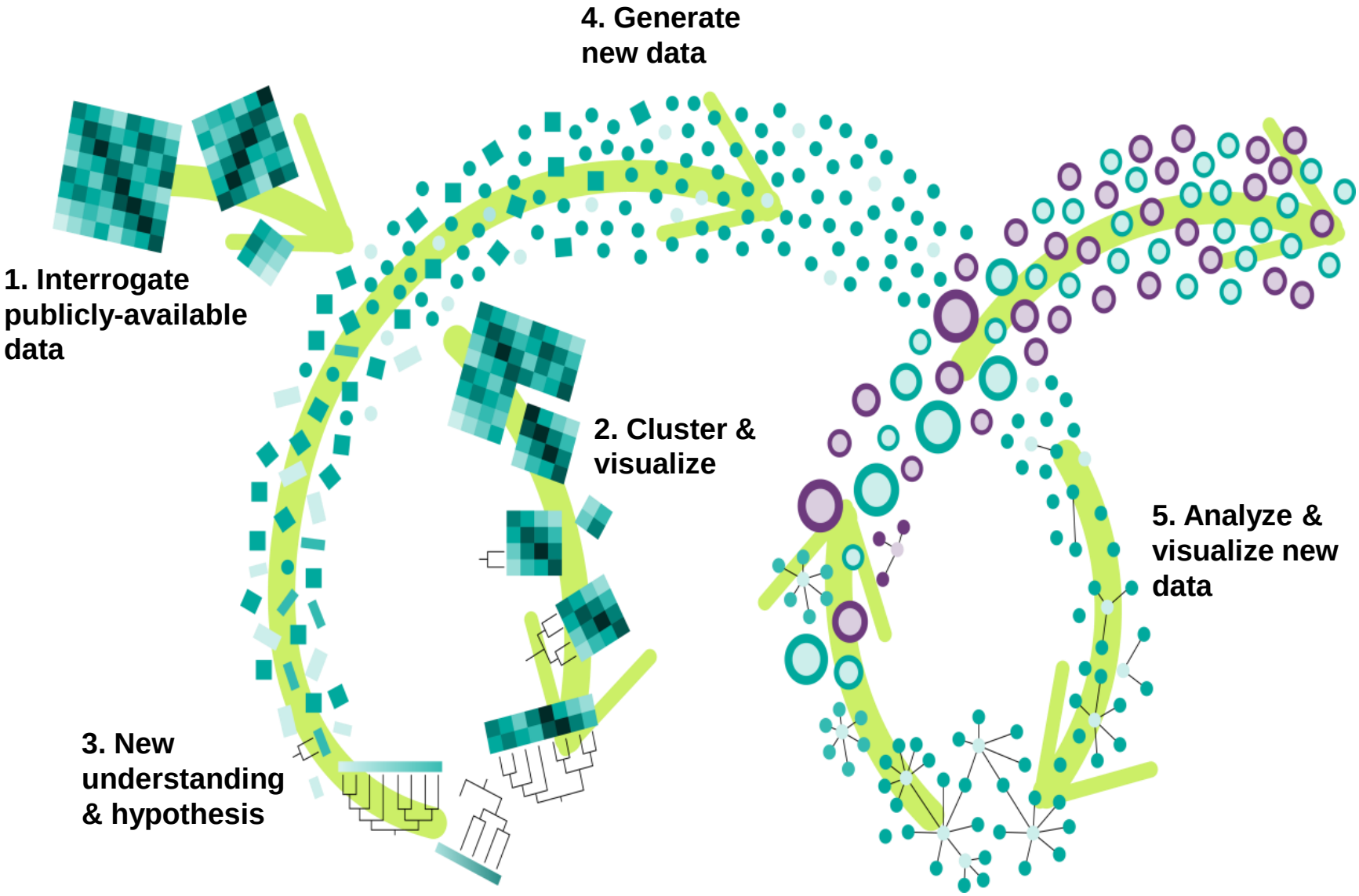
4. Generate new data
1. Interrogate publicly-available data
2. Cluster & visualize
5. Analyze & visualize new data
3. New understanding & hypothesis

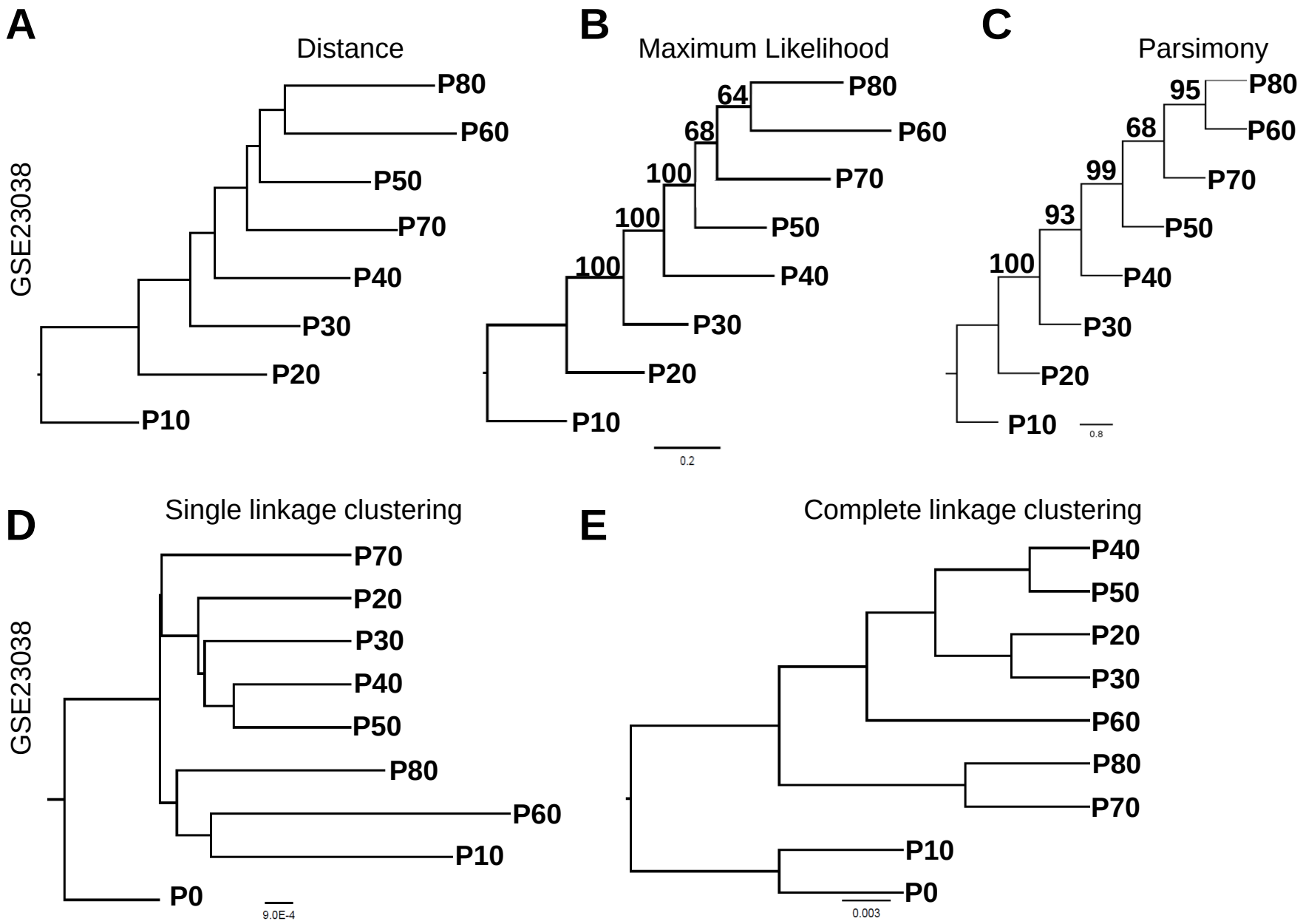
A
Distance
GSE23038
P80
P60
P50
P70
P40
P30
P20
P10
B
Maximum Likelihood
64
68
100
100
100
P80
P60
P70
P50
P40
P30
P20
P10
0.2
C
Parsimony
95
68
99
93
100
P80
P60
P70
P50
P40
P30
P20
P10
0.8
D
Single linkage clustering
GSE23038
P70
P20
P30
P40
P50
P80
P60
P10
P0
9.0E-4
E
Complete linkage clustering
P40
P50
P20
P30
P60
P80
P70
P10
P0
0.003

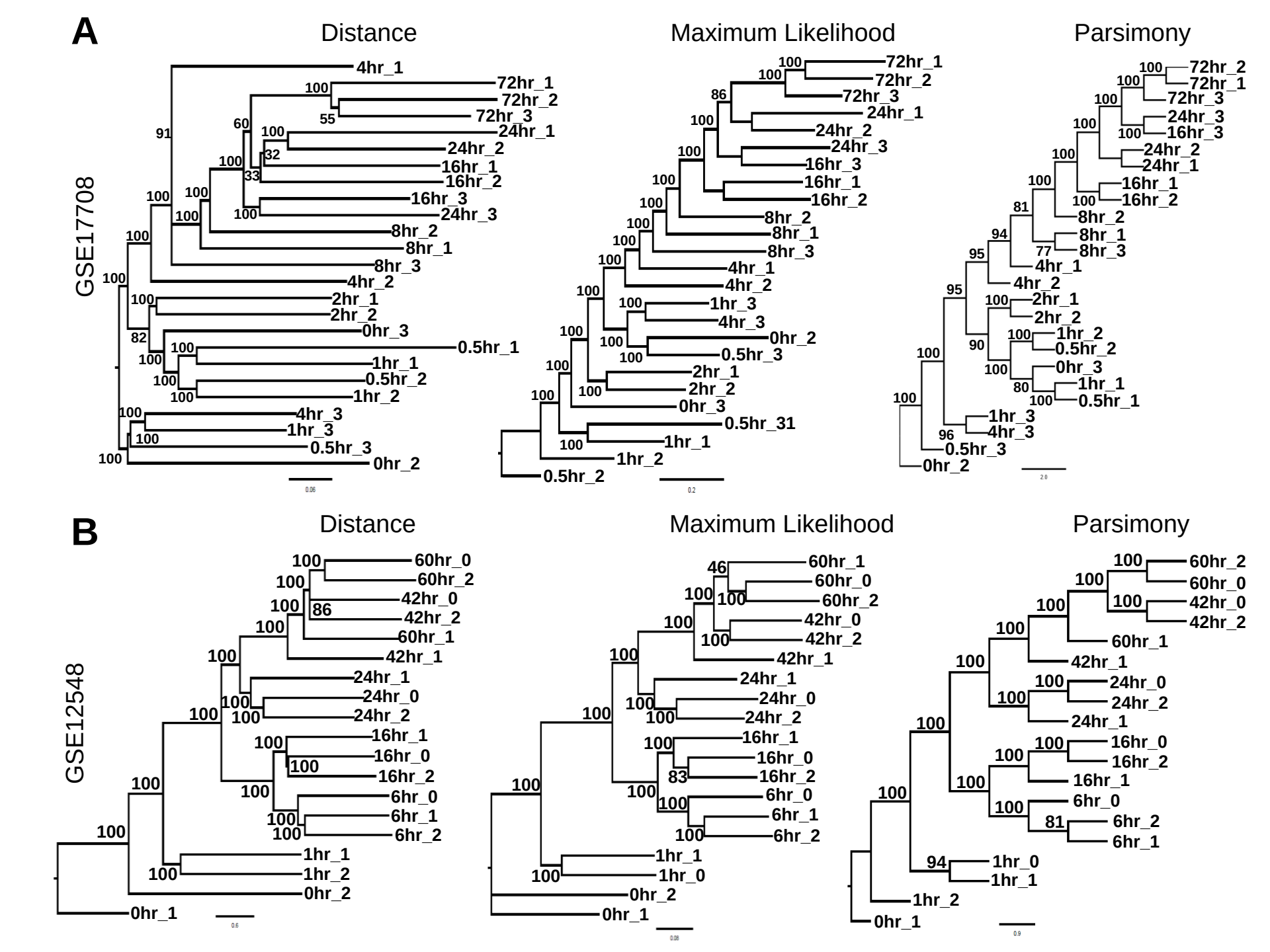
A
Distance
Maximum Likelihood
Parsimony
GSE17708
4hr_1
72hr_1
72hr_2
72hr_3
24hr_1
24hr_2
16hr_1
16hr_2
16hr_3
24hr_3
8hr_2
8hr_1
8hr_3
4hr_2
2hr_1
2hr_2
0hr_3
0.5hr_1
1hr_1
0.5hr_2
1hr_2
4hr_3
1hr_3
0.5hr_3
0hr_2
72hr_1
72hr_2
72hr_3
24hr_1
24hr_2
24hr_3
16hr_3
16hr_1
16hr_2
8hr_2
8hr_1
8hr_3
4hr_1
4hr_2
1hr_3
4hr_3
0hr_2
0.5hr_3
2hr_1
2hr_2
0hr_3
0.5hr_31
1hr_1
1hr_2
0.5hr_2
72hr_2
72hr_1
72hr_3
24hr_3
16hr_3
24hr_2
24hr_1
16hr_1
16hr_2
8hr_2
8hr_1
8hr_3
4hr_1
4hr_2
2hr_1
2hr_2
1hr_2
0.5hr_2
0hr_3
1hr_1
0.5hr_1
1hr_3
4hr_3
0.5hr_3
0hr_2
B
Distance
Maximum Likelihood
Parsimony
GSE12548
60hr_0
60hr_2
42hr_0
42hr_2
60hr_1
42hr_1
24hr_1
24hr_0
24hr_2
16hr_1
16hr_0
16hr_2
6hr_0
6hr_1
6hr_2
1hr_1
1hr_2
0hr_2
0hr_1
60hr_1
60hr_0
60hr_2
42hr_0
42hr_2
42hr_1
24hr_1
24hr_0
24hr_2
16hr_1
16hr_0
16hr_2
6hr_0
6hr_1
6hr_2
1hr_1
1hr_0
0hr_2
0hr_1
60hr_2
60hr_0
42hr_0
42hr_2
60hr_1
42hr_1
24hr_0
24hr_2
24hr_1
16hr_0
16hr_2
16hr_1
6hr_0
6hr_2
6hr_1
1hr_0
1hr_1
1hr_2
0hr_1

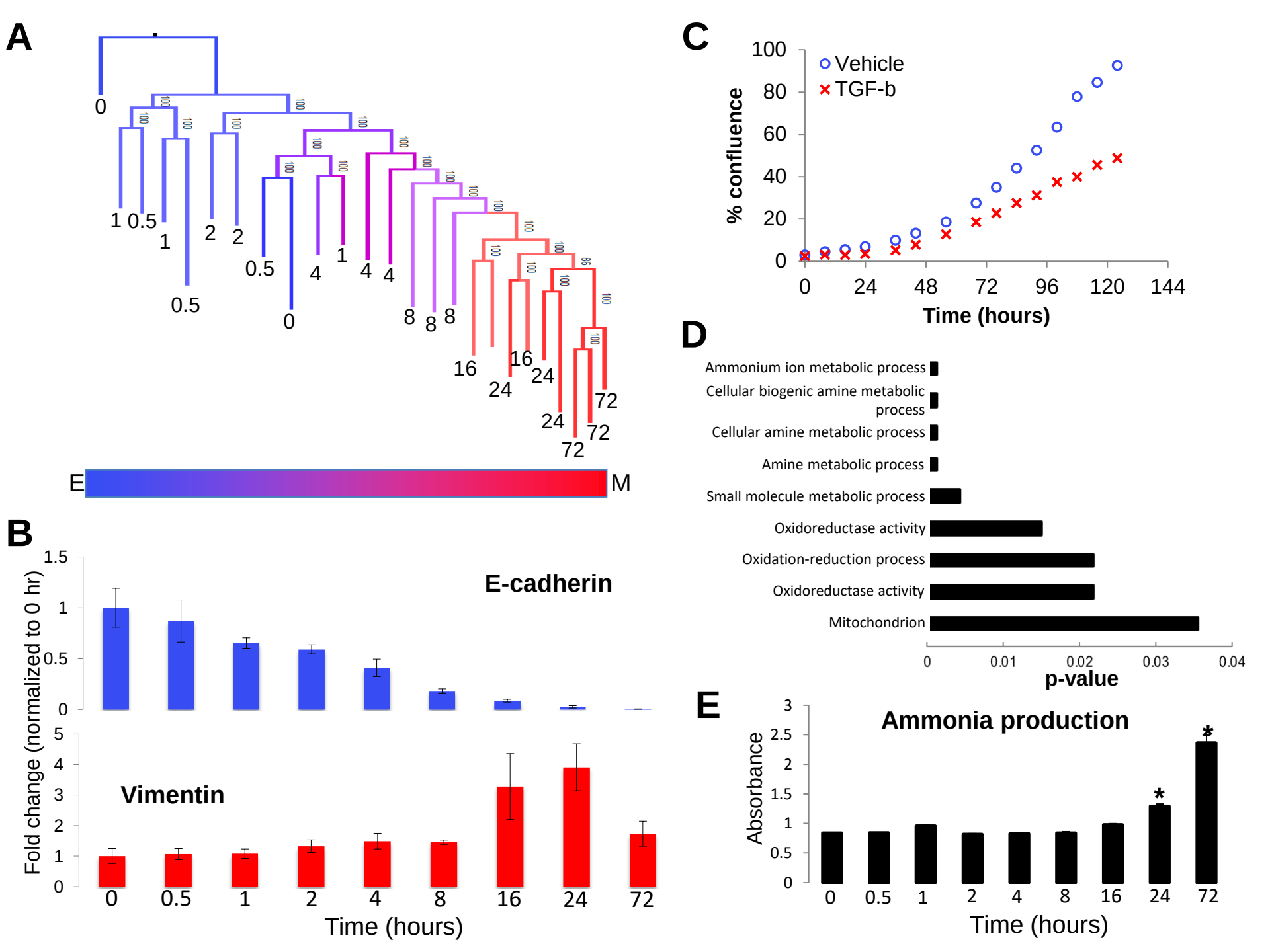
A
0
1
0.5
1
0.5
2
2
0.5
0
4
1
4
4
8
8
8
16
24
16
24
24
72
72
72
E
M
B
E-cadherin
Vimentin
Fold change (normalized to 0 hr)
Time (hours)
0
0.5
1
2
4
8
16
24
72
C
Vehicle
TGF-b
% confluence
Time (hours)
D
Ammonium ion metabolic process
Cellular biogenic amine metabolic process
Cellular amine metabolic process
Amine metabolic process
Small molecule metabolic process
Oxidoreductase activity
Oxidation-reduction process
Oxidoreductase activity
Mitochondrion
p-value
E
Ammonia production
Absorbance
Time (hours)

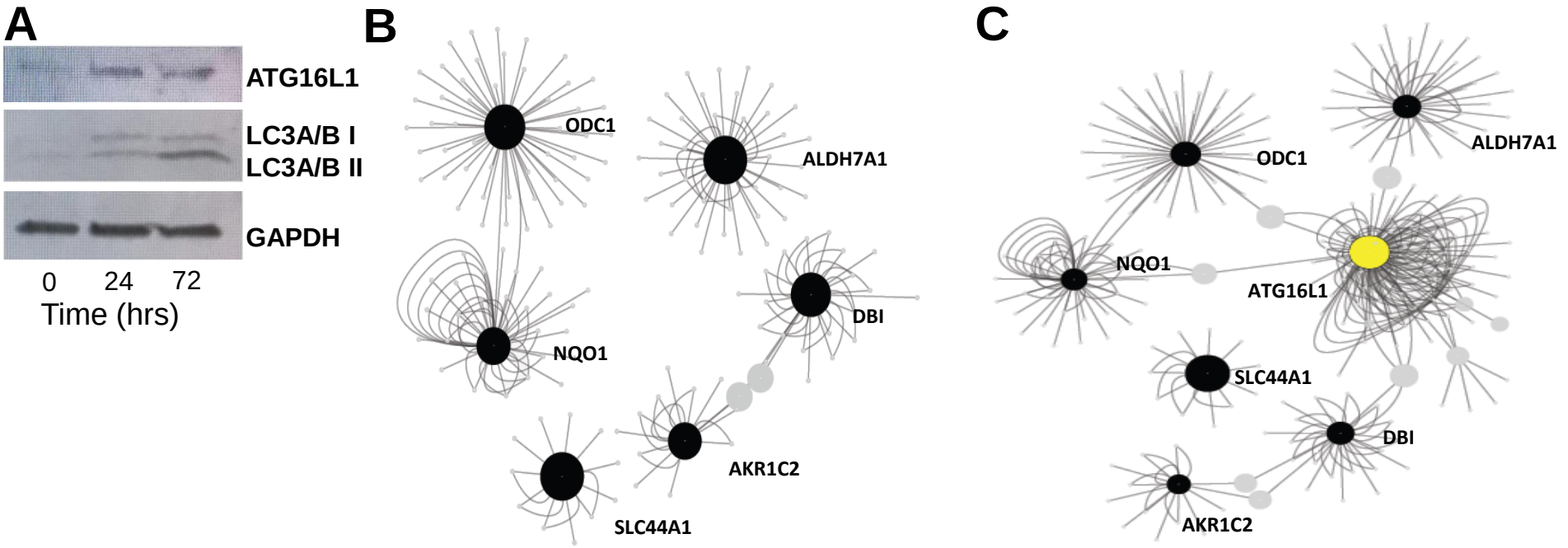
A
ATG16L1
LC3A/B I
LC3A/B II
GAPDH
0
24
72
Time (hrs)
B
ODC1
ALDH7A1
NQO1
DBI
AKR1C2
SLC44A1
C
ODC1
ALDH7A1
NQO1
ATG16L1
SLC44A1
DBI
AKR1C2

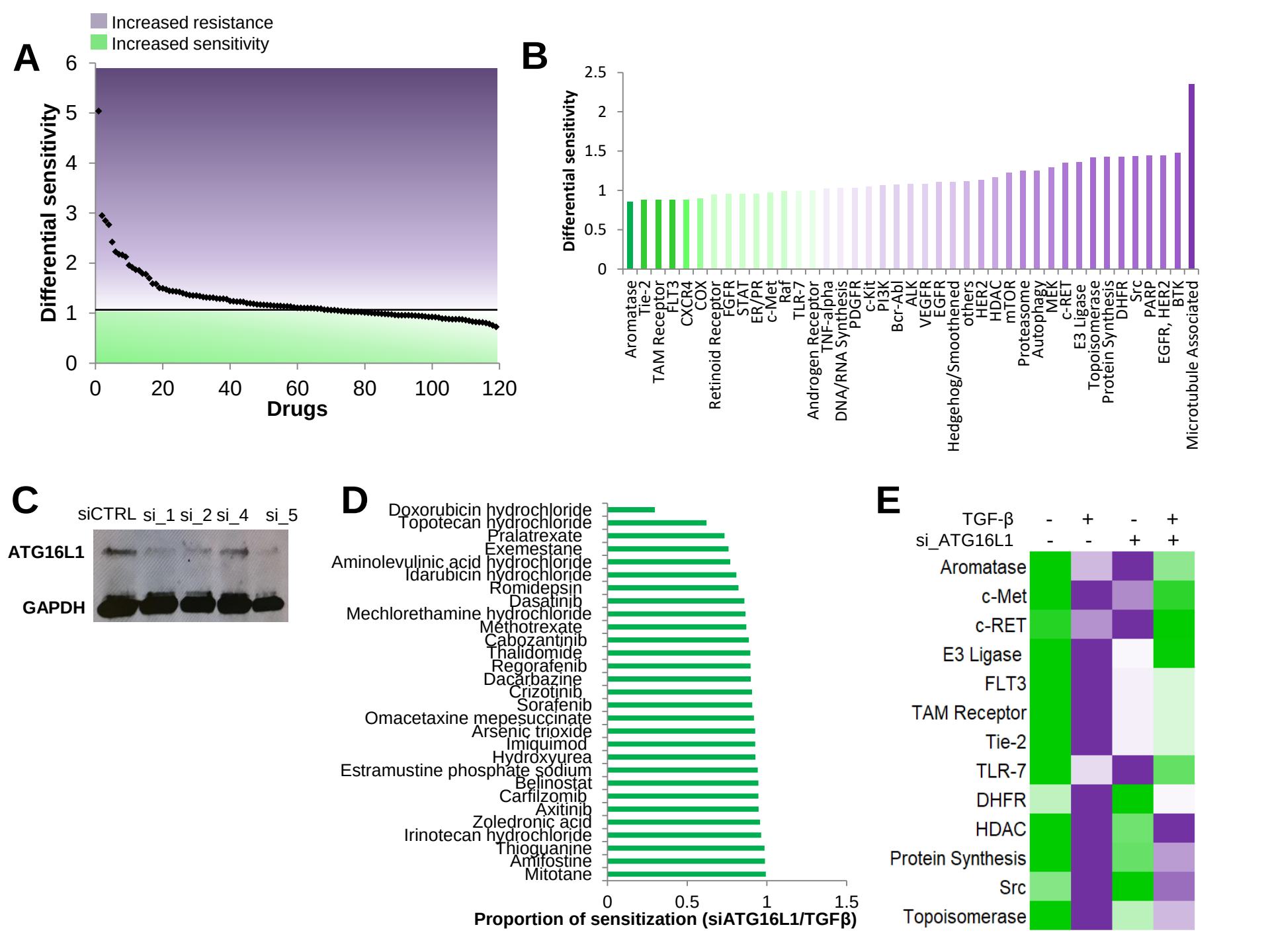
A
Increased resistance
Increased sensitivity
Differential sensitivity
Drugs
B
Differential sensitivity
Aromatase
Tie-2
TAM Receptor
FLT3
CXCR4
COX
Retinoid Receptor
FGFR
STAT
ER/PR
c-Met
Raf
TLR-7
Androgen Receptor
TNF-alpha
DNA/RNA Synthesis
PDGFR
c-Kit
PI3K
Bcr-Abl
ALK
VEGFR
EGFR
Hedgehog/Smoothened
others
HER2
HDAC
mTOR
Proteasome
Autophagy
MEK
c-RET
E3 Ligase
Topoisomerase
Protein Synthesis
DHFR
Src
PARP
EGFR, HER2
BTK
Microtubule Associated
C
siCTRL si_1 si_2 si_4 si_5
ATG16L1
GAPDH
D
Doxorubicin hydrochloride
Topotecan hydrochloride
Pralatrexate
Exemestane
Aminolevulinic acid hydrochloride
Idarubicin hydrochloride
Romidepsin
Dasatinib
Mechlorethamine hydrochloride
Methotrexate
Cabozantinib
Thalidomide
Regorafenib
Dacarbazine
Crizotinib
Sorafenib
Omacetaxine mepesuccinate
Arsenic trioxide
Imiquimod
Hydroxyurea
Estramustine phosphate sodium
Belinostat
Carfilzomib
Axitinib
Zoledronic acid
Irinotecan hydrochloride
Thioguanine
Amifostine
Mitotane
Proportion of sensitization (siATG16L1/TGFβ)
E
TGF-β
si_ATG16L1
Aromatase
c-Met
c-RET
E3 Ligase
FLT3
TAM Receptor
Tie-2
TLR-7
DHFR
HDAC
Protein Synthesis
Src
Topoisomerase

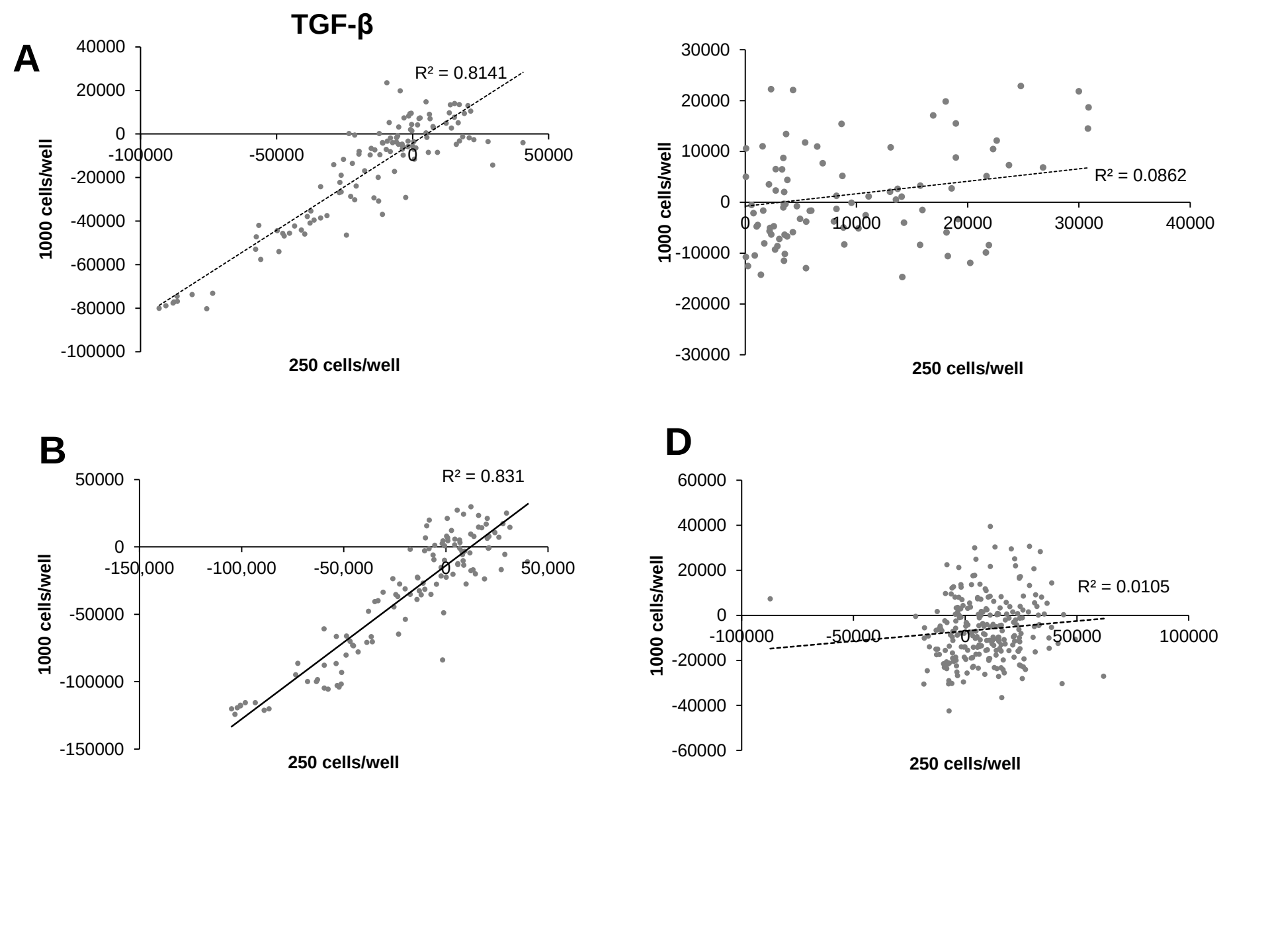
TGF-β
A
R² = 0.8141
1000 cells/well
250 cells/well
40000
20000
0
-20000
-40000
-60000
-80000
-100000
-100000
-50000
0
50000
R² = 0.0862
30000
20000
10000
0
-10000
-20000
-30000
0
10000
20000
30000
40000
B
R² = 0.831
50000
0
-50000
-100000
-150000
-150,000
-100,000
-50,000
0
50,000
D
R² = 0.0105
60000
40000
20000
0
-20000
-40000
-60000
-100000
-50000
0
50000
100000

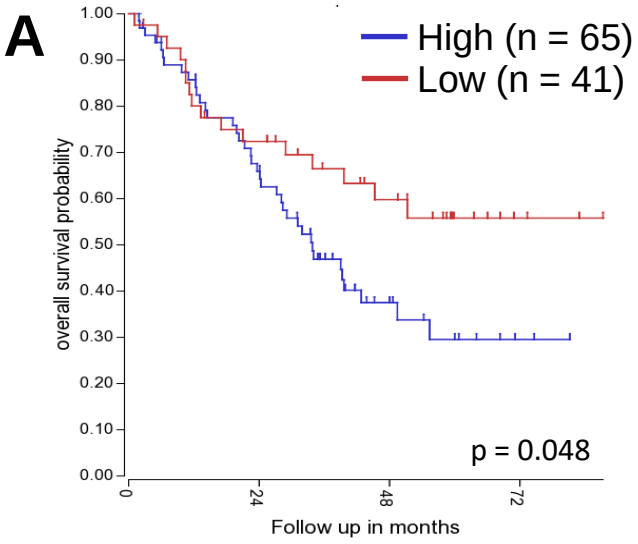
A
High (n = 65)
Low (n = 41)
overall survival probability
1.00
0.90
0.80
0.70
0.60
0.50
0.40
0.30
0.20
0.10
0.00
0
24
48
72
Follow up in months
p = 0.048

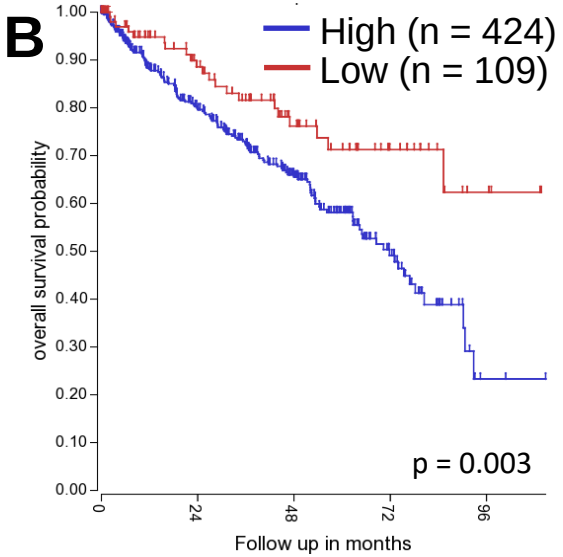
B
High (n = 424)
Low (n = 109)
overall survival probability
1.00
0.90
0.80
0.70
0.60
0.50
0.40
0.30
0.20
0.10
0.00
0
24
48
72
96
Follow up in months
p = 0.003

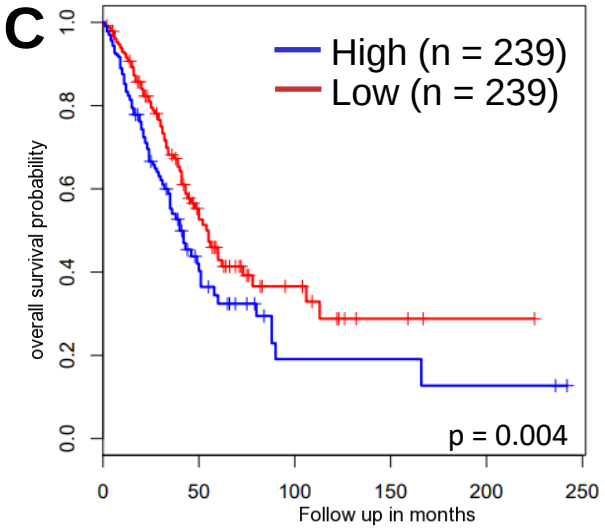
C
High (n = 239)
Low (n = 239)
overall survival probability
1.0
0.8
0.6
0.4
0.2
0.0
0
50
100
150
200
250
Follow up in months
p = 0.004

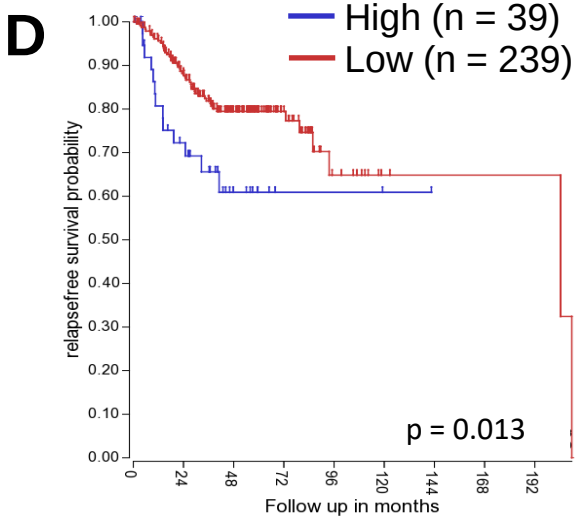
D
High (n = 39)
Low (n = 239)
relapsefree survival probability
1.00
0.90
0.80
0.70
0.60
0.50
0.40
0.30
0.20
0.10
0.00
0
24
48
72
96
120
144
168
192
Follow up in months
p = 0.013

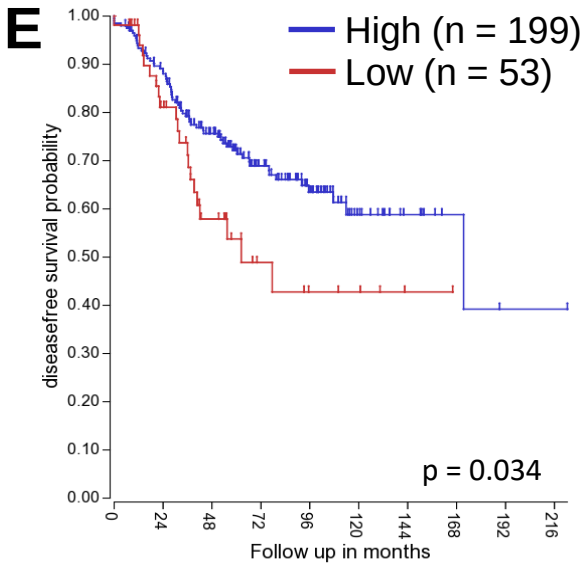
E
High (n = 199)
Low (n = 53)
diseasefree survival probability
1.00
0.90
0.80
0.70
0.60
0.50
0.40
0.30
0.20
0.10
0.00
0
24
48
72
96
120
144
168
192
216
Follow up in months
p = 0.034